J Appl Electrochem (2014) 44:1171–1177
DOI 10.1007/s10800-014-0735-6

RESEARCH ARTICLE

# Effects of a graphene nanosheet conductive additive on the high-capacity lithium-excess manganese–nickel oxide cathodes of lithium-ion batteries

**Wen-Chin Chen · Cheng-Yu Hsieh · Yu-Ting Weng · Fu-Sheng Li · Hung-Chun Wu · Nae-Lih Wu**

Received: 26 April 2014 / Accepted: 18 August 2014 / Published online: 26 August 2014


**Abstract** This study examines the effects of a graphene nanosheet (GNS) conductive additive on the performance of a highly packed (2.5 g $cm^{-3}$) lithium-ion battery cathode containing 92 wt% $Li_{1.1}(Mn_{0.6}Ni_{0.4})_{0.9}O_2$ microspheres (approximately 6 μm in diameter). GNSs, approximately 2.0 nm thick and 0.5–1.0 μm in width, are introduced into an electrode slurry in the form of a dispersion in N-Methyl-2-pyrrolidone. They are substantially smaller than the oxide particles; therefore, their presence exerts no adverse influence on the packing density of the electrode. A small quantity of the GNS additive (≤200 ppm relative to the oxide mass) can significantly increase the overall electronic conductance and improve the conductance uniformity of the oxide electrode, leading to reduced polarization and enhanced specific capacity and rate performance. However, the GNS additive also promotes solid-electrolyte interphase formation, resulting in resistance buildup and capacity deterioration upon cycling. This study is the first to identify such an adverse effect caused by a graphene additive. The interplay between the positive and negative effects has led to an optimal GNS additive content of approximately 100 ppm, enhancing both the rate and cycle life performance.

W.-C. Chen · Y.-T. Weng · F.-S. Li · N.-L. Wu (✉)
Department of Chemical Engineering, National Taiwan University, Taipei 106, Taiwan
e-mail: nlw001@ntu.edu.tw

C.-Y. Hsieh
Enerage Incorporation, Wujie Township, Yilan County 26841, Taiwan

H.-C. Wu
Industrial Technology Research Institute (ITRI), Hsinchu, Taiwan

**Keywords** Graphene · Lithium-excess layered oxide · Cathode · Conductive additive

## 1 Introduction

Lithium-ion batteries (LIBs) are expected to continue playing a crucial role in energy storage in the next decade. Research on advanced lithium-ion secondary batteries has trended toward high energy and power densities. For cathode materials, a class of layered lithium-excess manganese transition metal oxides (LeMOs), with a general formula of $Li_{1+x}(Mn,M)_{1-x}O_2$, has drawn increased attention because their capacities exceed 200 $mAhg^{-1}$ [1–3]. In LeMOs, an excess lithium ion promotes the presence of intergrown $Li_2MnO_3$ within the $Li(Mn,M)O_2$ matrix to form a layered composite structure. $Li_2MnO_3$ is transformed into electrochemically active $MnO_2$ through the removal of the $Li^+$ ion on charging above 4.5 V (vs. $Li/Li^+$) and stabilizes the layered structure in deep lithiation and delithiation cycles [4, 5]. The major disadvantages of LeMO cathodes, however, include electrolyte decomposition at high potentials and poor electronic conductivity [4]. Electrolyte decomposition reduces Coulombic efficiency and cycle life, and poor electronic conductivity limits capacity and rate performance.

A preliminary study determined that LeMO particles easily decompose on contact with hydrocarbons at high temperatures (>400 °C). Performing thermal carbon coating of the oxide without reducing its specific capacity is impossible; therefore, the electronic conductivity of a LeMO electrode relies mainly on the characteristics and distribution of the carbon additives that form the conductive network therein. Graphene has attracted considerable interest for use as a conductive additive in electrochemical

electrodes because of its excellent electronic conductivity along the basal plane, large surface area, and flexibility [6, 7]. Studies have reported that wrapping nano- and submicron active material particles in large graphene sheets can substantially improve rate performance [8–11]; however, this approach is inadequate for achieving high-capacity electrodes for two reasons. First, previous studies have used a large amount of graphene sheets along with other carbon additives (>10 wt%) to enhance rate performance but this approach unavoidably compromises the capacity of the entire electrode because of the reduced active material content. Second, large graphene sheets have a low packing density, which reduces the capacity and energy densities of the electrode. However, these concerns have largely been overlooked.

In this study, we assessed a new approach in which a small amount (≤200 ppm) of graphene nanosheets (GNSs; approximately 2.0 nm thick) is applied to a highly packed (2.5 g $cm^3$) cathode that contains 92 wt% spherical and micron-sized $Li_{1.1}(Mn_{0.6}Ni_{0.4})_{0.9}O_2$ and only 4 wt% carbon conductive additives. The spherical geometry and applied particle dimensions are intended to achieve a high electrode packing density [12–14]. The GNS additive was introduced into the electrode slurry in the form of a dispersion in N-Methyl-2-pyrrolidone (NMP). In contrast to previous studies [8–11], the GNSs in the current study exhibited dimensions (0.5–1.0 μm) that are substantially smaller than those of the oxide particles within the electrode. The combination of small quantity and dimensions ensures that the presence of the GNS additive exerts no adverse influence on the packing density of the oxide electrode. The results showed that the GNS additive, even at such a small quantity, can substantially improve the capacity and rate performance of the oxide electrode. However, the GNS additive promotes solid-electrolyte interphase (SEI) formation and, when used in large amounts, can lead to fast capacity fading upon cycling.

## 2 Experimental

Micro-sized and nearly spherical $Li_{1.1}(Mn_{0.6}Ni_{0.4})_{0.9}O_2$ particles were synthesized using a coprecipitation–calcination process, as described in detail previously [15]. Graphene was supplied in the form of a dispersion in NMP (Enerage Inc.). The electrode slurry was fabricated by mixing $Li_{1.1}(Mn_{0.6}Ni_{0.4})_{0.9}O_2$ powder, polyvinylidenedifluoride (PVDF), graphite flakes (KS-6, TIMCAL), and carbon black (CB; Super P, TIMCAL) at mass ratios of 92:4:2:2 in the graphene-containing NMP. Slurries with GNS-to-oxide mass ratios of 50, 100, and 200 ppm were prepared. The slurries were coated onto Al current collectors and dried at 150 °C in vacuum for 6 h.

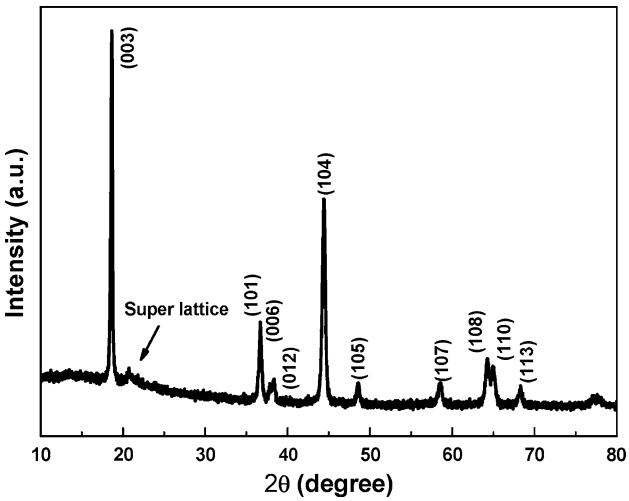


**Fig. 1** XRD pattern of the $Li_{1.1}(Ni_{0.4}Mn_{0.6})_{0.9}O_2$ cathode

The morphologies of prepared samples were examined using a scanning electron microscope (SEM; JEOL JSM-7600F) and a field-emission transmission electron microscope (Hitachi H-7100 TEM), whereas the crystal structure and phase composition were identified using X-ray diffraction (XRD) on a diffractometer (RigakuUltima IV) with Cu Kα X-ray radiation. The thickness of the graphene sheets was measured using an atomic force microscope (AFM; Nanosurf Flex) in a tapping mode at a scan speed of 0.5 Hz.

For electrochemical characterization, the electrode sheets were punched into disks, 1.2 cm in diameter, for assembly into coin cells. The coin cells consisted of a $Li_{1.1}(Mn_{0.6}Ni_{0.4})_{0.9}O_2$ electrode, a lithium foil disk as the counter electrode, and an electrolyte of 1 M $LiPF_6$ in a 1:2 v/v mixture of ethylene carbonate and dimethyl carbonate. A polypropylene porous membrane was used as the separator. All of the cells were assembled in a dry room where the dew point was maintained between −40 and −45 °C. The cells were charged and discharged at a current density of 10 mA $g^{-1}$ between 2.0 and 4.9 V for the first cycle and then at applied current densities between 2.0 and 4.6 V for the subsequent cycles. Current density was calculated based on the oxide content in the electrode. Alternating current (AC) electrochemical impedance was measured after charging the electrode to 4.0 V. The amplitude was 10 mV, and the frequency ranged from 200 to 10 mHz. Electrode resistance was determined by a home-made four-probe resistance-measuring device.

## 3 Results and discussion

$Li_{1.1}(Mn_{0.6}Ni_{0.4})_{0.9}O_2$ can be considered as a composite of $Li_2MnO_3$ and $LiNi_{0.5}Mn_{0.5}O_2$, and can therefore be

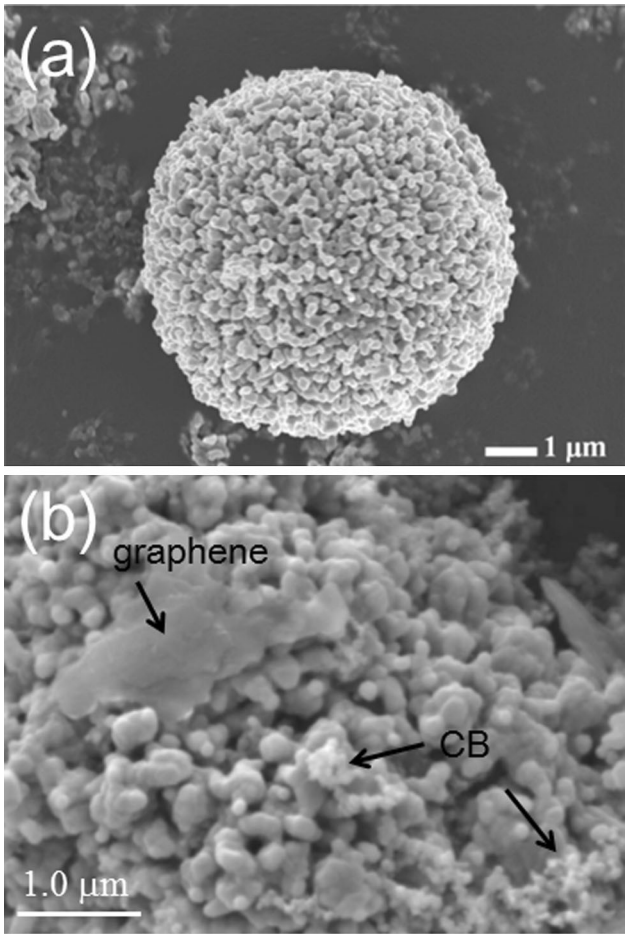


**Fig. 2** **a** SEM micrograph of the spherical $Li_{1.1}(Ni_{0.4}Mn_{0.6})_{0.9}O_2$ particle; **b** SEM micrograph showing typical configurations of GNS and CB on the $Li_{1.1}(Mn_{0.6}Ni_{0.4})_{0.9}O_2$ particle surface

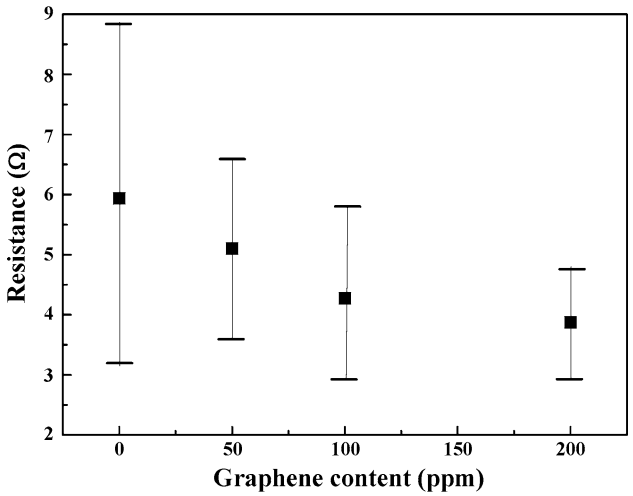


**Fig. 4** Electrode resistance versus GNS content: shown are resistance data measured by the four-probe method at five randomly selected locations over a 20 cm × 20 cm area for every one of the electrodes

expressed as $0.2Li_2MnO_3{\cdot}0.8LiNi_{0.5}Mn_{0.5}O_2$. X-ray diffraction of the powder showed strong peaks characteristic of layered $LiMO_2$ structures (Fig. 1) and weak superstructure peaks (arrow in Fig. 1) arising from the presence of the intergrown $Li_2MnO_3$. The $Li_{1.1}(Mn_{0.6}Ni_{0.4})_{0.9}O_2$ particles exhibited nearly spherical morphology (Fig. 2a), an average particle size of approximately 6 μm, and a specific surface area of 2.20 $m^2\ g^{-1}$. The AFM image (Fig. 3a) showed the morphology of the GNS to be sheet-like with widths ranging from 0.5 to 1.0 μm, which is much smaller than the size of the $Li_{1.1}(Mn_{0.6}Ni_{0.4})_{0.9}O_2$ particles. Thickness analysis (Fig. 3b) revealed a GNS thickness of approximately 2 nm.

Figure 2b shows the typical configuration of the GNS on the oxide surface. The GNS could lie conformably on the oxide particle surface because of its flexibility, forming a "plane contact" with the surface. By contrast, the CB particles, also shown in Fig. 2b, tended to agglomerate and form "point contacts" either with the oxide surface or among themselves. For the same amount of carbon additive, the GNS can provide a greater contact area with the oxide surface. Moreover, electric currents can flow along the highly conductive basal plane in the case of GNSs, but must flow through numerous resistive particle-to-particle contacts in the case of CB particles. Therefore, GNSs are expected to be more efficient than CB particles for serving as a conductive additive.

Four-probe resistance measurement was conducted to determine the resistances of the electrodes. Figure 4

**Fig. 3** **a** Atomic force micrograph of a single graphene sheet; **b** thickness measurement

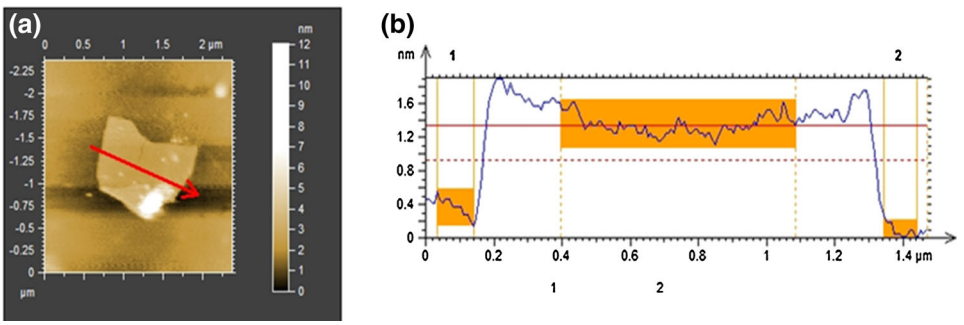

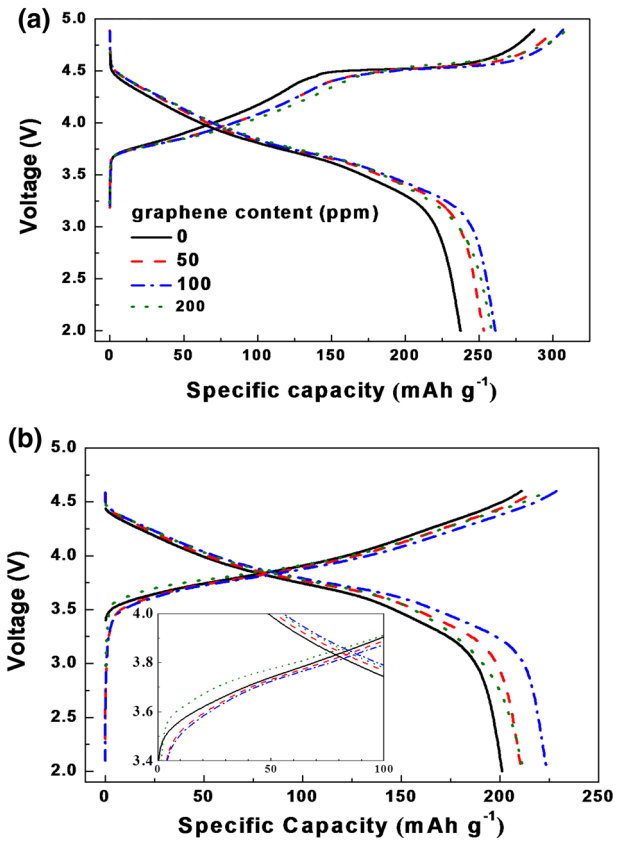


**Fig. 5** Electrochemical properties of the $Li_{1.1}(Mn_{0.6}Ni_{0.4})_{0.9}O_2$ electrodes containing different amounts of GNS additives: **a** voltage plots of the first cycle; **b** voltage plots of the second cycle

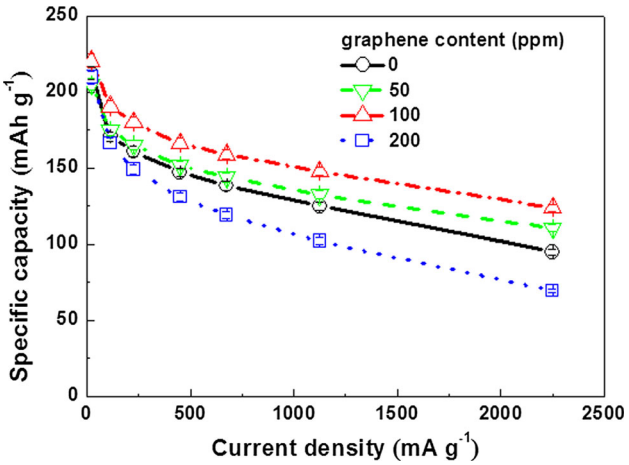


**Fig. 6** Specific discharge capacities at different current densities for the $Li_{1.1}(Mn_{0.6}Ni_{0.4})_{0.9}O_2$ electrodes containing different amounts of GNS additives

summaries the data acquired from five measurements at different locations for every one of the electrodes. As shown, the electrode without GNS shows a very wide range of variation in resistance. This non-uniformity may be due to agglomeration of the CB particles (Fig. 2b). With increasing amount of GNS addition, the average resistance decreased and the extent of variation also became narrower. The data indicate that GNS addition not only enhances the overall conductance but also substantially improves the conductance uniformity of the electrode. The latter effect may be attributed to the none-agglomerating nature of the GNSs, which enables homogeneous distribution of the GNSs within the electrode.

Figure 5a presents a comparison of the first charge/discharge cycle of the electrodes. For each charge plot, the capacity associated with the initial slope between 3.7 and 4.5 V arises from oxidation of $Ni^{2+}$ to $Ni^{4+}$, whereas the capacity associated with the plateau at 4.5 V is due to the removal of lithium ions from $Li_2MnO_3$ domains producing activated $MnO_2$. The large first-cycle capacity loss is mainly caused by the electrochemical removal of two lithium ions per $Li_2MnO_3$ during charge and the reinsertion of only one lithium ion into the resulting $MnO_2$ component during discharge. Electrolyte decomposition at high voltages after charging can also be a contributing factor [4, 5].

The 0 ppm electrode exhibited the highest charge voltage and the lowest discharge voltage (Fig. 5a), indicating the largest polarization among these oxide electrodes. The polarization decreased as the GNS content increased. Furthermore, the GNS-modified electrodes exhibited discharge capacities up to 9.7 % higher than that of non-GMS-modified electrode. The reduced polarization and increased capacity may be attributed to the enhanced electronic conductance and improved conductance uniformity (Fig. 4) of the electrode by the addition of GNSs. In the 0 ppm electrode, a part of the electrode reaches the cut-off voltage limit earlier than the rest because of poor conductive networking, resulting in a smaller specific capacity.

For the second cycle (2.0–4.6 V; Fig. 5b), the 0 ppm electrode continued to have the smallest capacity. The 200 ppm electrode, however, had the highest charge voltage during the first half of the charge cycle (inset, Fig. 5b). In addition, the 200 ppm electrode had a considerably lower discharge capacity than the 100 ppm electrode did, although they had nearly the same capacity in the first cycle. These data suggested a faster resistance buildup in the 200 ppm electrode than in the other electrodes.

Rate performance test was performed by charging the electrodes at 20 mA $g^{-1}$ and then discharging at different current densities that ranged from 20 to 2250 mA $g^{-1}$. Figure 6 plots the specific discharge capacity as a function of current density. Examples of discharge voltage plots are shown in Fig. 7. As the GNS content increased from 0 to 100 ppm, the rate performance also steadily increased; when the GNS content reached 200 ppm, the rate

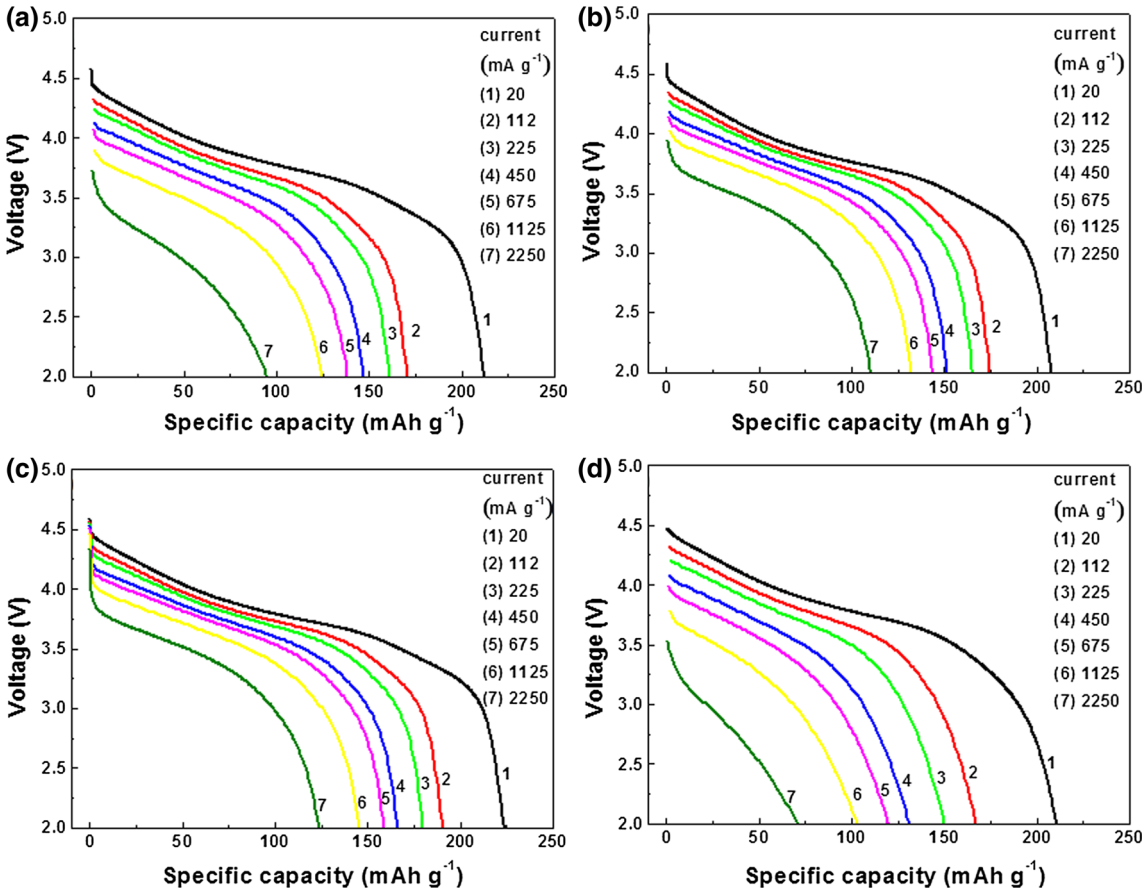


**Fig. 7** Discharge voltage plots at different current rates for the electrodes containing GNS additives of **a** 0 ppm; **b** 50 ppm; **c** 100 ppm; and **d** 200 ppm

performance dropped rapidly. Although the 200 ppm electrode started with a higher capacity than did the 0 ppm electrode at 20 mA $g^{-1}$, its specific capacity declined much faster as the current density increased. In Fig. 7, the 200 ppm electrode clearly shows the highest degree of polarization among all of the electrodes at high current rates.

AC electrochemical impedance analysis was conducted following the rate performance test. The spectra were recorded during the charge cycle at 4.0 V (state-of-charge approximately 54–57 %). As shown in Fig. 8, the Nyquist plots of these electrodes exhibited similar profiles, including two semicircles over the high-to-medium frequency range and an inclined straight line over the low-frequency range. The first intercept on the real-part axis $Z_{re}$ was attributed to bulk electrolyte resistance, whereas the widths of the two semicircles on the $Z_{re}$ axis were considered to be surface film (or SEI) resistance, $R_s$, and the overall charge-transfer resistance, $R_{ct}$, respectively. The inclined line corresponded to the Warburg impedance, which accounted for lithium ion diffusion within the oxide particles. By contrast, $R_s$ initially decreased slightly as the

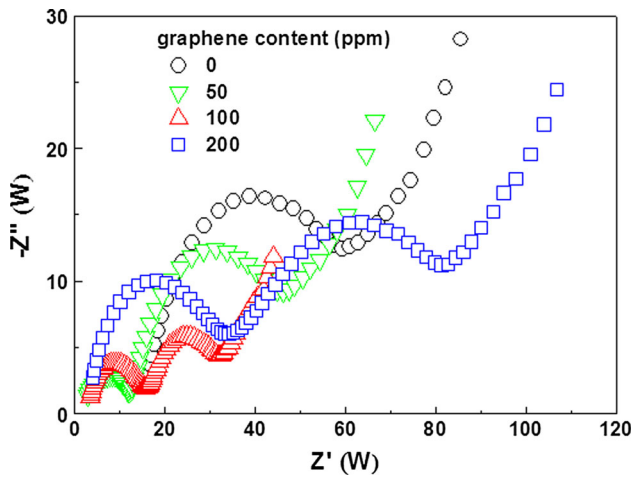


**Fig. 8** Nyquist plots on charge to 4 V for the $Li_{1.1}(Mn_{0.6}Ni_{0.4})_{0.9}O_2$ electrodes containing different amounts of GNS additives

GNS content increased from 0 to 50 ppm, and then increased steadily as the GNS content increased from 50 to 200 ppm. In particular, the 200 ppm electrode exhibited a

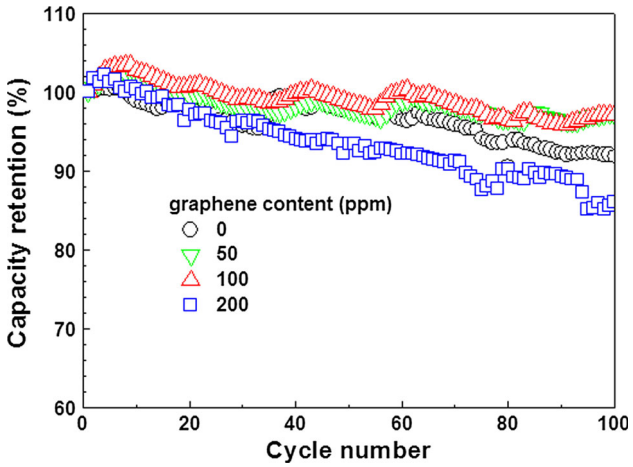


**Fig. 9** Cycling performance (current density: 225 mA $g^{-1}$) of the $Li_{1.1}(Mn_{0.6}Ni_{0.4})_{0.9}O_2$ electrodes containing different amounts of GNS additives

value of $R_s$ that was more than twice that of the other electrodes. The data suggested that the presence of GNSs promotes the formation of SEI layers.

The $R_{ct}$ of a particulate-type electrode should include the generally recognized electron-transfer resistance at the solid-electrolyte interface and the resistances associated with the conductive network within the active layer [16]. The impedance data showed steady reduction in $R_{ct}$ as the GNS content increased from 0 to 100 ppm (Fig. 8). This can be attributed to improved overall conductance of the electrode by increasing the GNS content. By contrast, $R_{ct}$ suddenly increased when the GNS content was raised to 200 ppm. The $R_{ct}$ of the 200 ppm electrode was close to that of the 0 ppm electrode. We inferred that, although increasing GNS content enhanced the conductance of the 200 ppm electrode, the fast buildup of the insulating SEI layer, as indicated by its high $R_s$, deteriorated conductance between oxide particles and hence upset the GNS-enabled conductance improvement. Finally, the 100 ppm electrode exhibited the lowest overall resistance ($R_s + R_{ct}$), thus confirming that this electrode demonstrated the highest rate performance (Fig. 6).

Figure 9 display plots of capacity retention as a function of cycle number for cycling at 225 mA $g^{-1}$ for 100 cycles. The 0 ppm electrode retained 92 % capacity. Both the 50 and 100 ppm electrodes exhibited 97 % capacity retention, which was superior to that of the 0 ppm electrode. By contrast, the 200 ppm electrode showed the most substantial capacity fading and retained only 86 % capacity. Figure 10a, b, c compare the surface morphologies of the cycled electrodes. For the 0 ppm electrode, the small oxide grains remained clearly visible (Fig. 10a). The morphologies of the 50 and 100 ppm electrodes were similar, and the

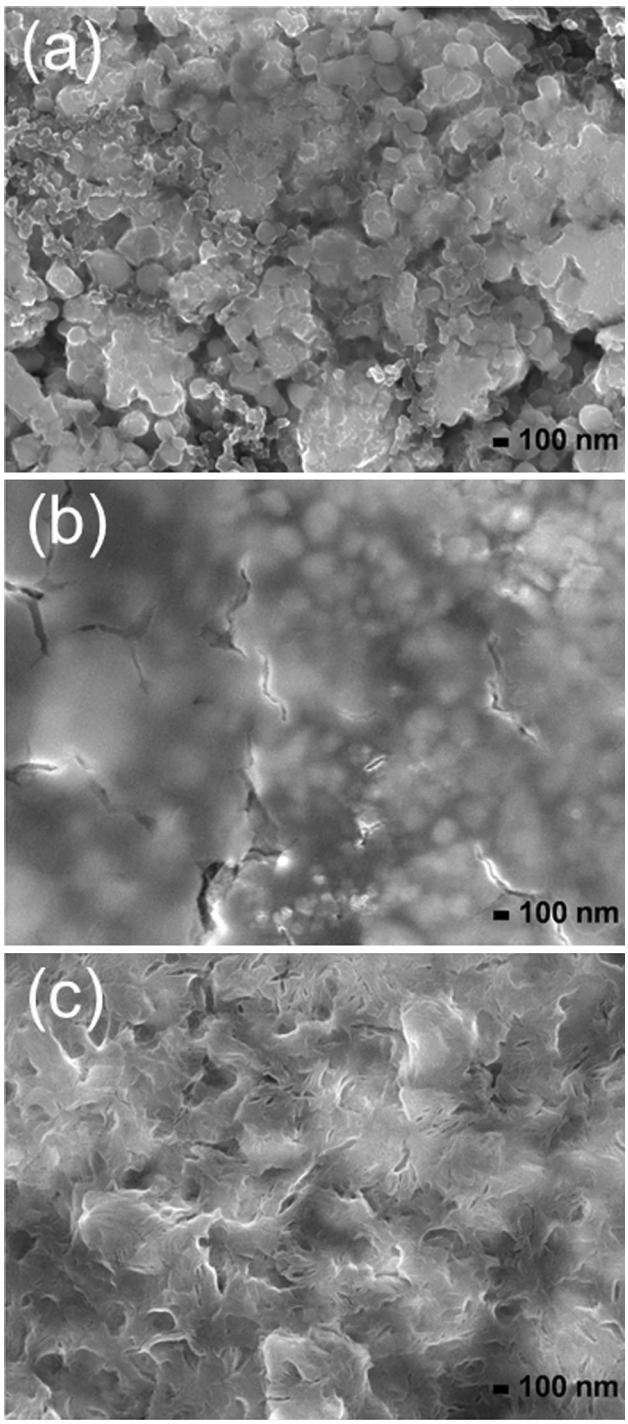


**Fig. 10** **a** SEM micrograph of the surfaces of the 0 ppm electrode after 100 cycles; **b** of the 100 ppm electrode; **c** of the 200 ppm electrode

oxide grains were partially visible in both cases (Fig. 10b). The 200 ppm electrode was covered with a thick SEI deposit so that the oxide grains were no longer visible (Fig. 10c). The thickness of the SEI deposit clearly increased as the GNS content increased. This was

consistent with the impedance data (Fig. 8), which indicated increasing buildup of $R_s$ as the GNS content increased. The exact cause of the accelerated SEI formation requires elaborate chemical analysis and has not yet been determined. However, the carbon atoms at the edge sites of graphene layers are known to have much higher reactivity than those in basal planes; hence, we infer that the sharp edges of the GNSs may have acted as "catalytic" sites to facilitate electrolyte decomposition, particularly at high potentials.

In summary, we demonstrated that introduction of even a small ($\leq$200 ppm) amount of GNSs can have a considerable impact on the performance of highly packed $Li_{1.1}(Mn_{0.6}Ni_{0.4})_{0.9}O_2$ electrodes. The GNS addition not only enhanced the overall electronic conductance but also improved the conductance uniformity of the oxide electrode, resulting in reduced electrode polarization and enhanced specific capacity and rate performance. However, GNS addition was found to promote SEI formation. The interplay between these positive and negative effects led to an optimal amount of the additive at approximately 100 ppm, achieving both rate and cycle-life enhancements.

**Acknowledgments** This study was financially supported by the Ministry of Science and Technology (MOST), Taiwan, R.O.C, under contract number NSC 102-3113-P-002-043. Thanks to S.-J. Ji of MOST (National Taiwan University) for the assistance in SEM analysis.

## References

1. Lu Z, Macneil DD, Dahn JR (2001) Layered cathode materials $Li[Ni_xLi_{(1/3-2x/3)}Mn_{(2/3-x/3)}]O_2$ for lithium-ion batteries. Electrochem Solid-State Lett 4:A191–A194
2. Thackeray MM, Johnson CS, Vaughey JT, Li N, Hackney SA (2005) Advances in manganese-oxide 'composite' electrodes for lithium-ion batteries. J Mater Chem 15:2257–2267
3. Xu B, Fell CR, Chi M, Meng YS (2011) Identifying surface structural changes in layered Li-excess nickel manganese oxides in high voltage lithium ion batteries: a joint experimental and theoretical study. Energy Environ Sci 4:2223–2233
4. Johnson CS, Kim JS, Lefief C, Li N, Vaughey JT, Thackeray MM (2004) The significance of the $Li_2MnO_3$ component in 'composite' $xLi_2MnO_3{\cdot}(1\text{-}x)LiMn_{0.5}Ni_{0.5}O_2$ electrodes. Electrochem Commun 6:1085–1091
5. Armstrong AR, Holzapfel M, Novák P, Johnson CS, Kang SK, Thackeray MM, Bruce PG (2006) Demonstrating oxygen loss and associated structural reorganization in the lithium battery cathode $Li[Ni_{0.2}Li_{0.2}Mn_{0.6}]O_2$. J Am Chem Soc 128:8694–8698
6. Geim AK, Novoselov KS (2007) The rise of grapheme. Nat Mater 6:183–191
7. Park S, Ruoff RS (2009) Chemical methods for the production of graphenes. Nat Nanotechnol 4:217–224
8. Song BH, Lai MO, Liu ZW, Liu HW, Lu L (2013) Graphene-based surface modification on layered Li-rich cathode for high-performance Li-ion batteries. J Mater Chem A 1:9954–9965
9. Prabakar SJR, Hwang YH, Lee B, Sohn KS, Pyo M (2013) Graphene-sandwiched $LiNi_{0.5}Mn_{1.5}O_4$ cathode composites for enhanced high voltage performance in Li ion batteries. J Electrochem Soc 160:A832–A837
10. Wang B, Wang DL, Wang QM, Liu TF, Guo CF, Zhao XS (2013) Improvement of the electrochemical performance of carbon-coated $LiFePO_4$ modified with reduced grapheme oxide. J Mater Chem A 1:135–144
11. Jiang R, Cui C, Ma H (2013) Using graphene nanosheets as a conductive additive to enhance the rate performance of spinel $LiMn_2O_4$ cathode material. Phys Chem Chem Phys 15:6406–6415
12. Deng H, Belharouak I, Sun YK, Amine K (2009) $Li_xNi_{0.25\text{-}}Mn_{0.75}O_y$ ($0.5 \leq x \leq 2$, $2 \leq y \leq 2.75$) compounds for high-energy lithium-ion batteries. J Mater Chem 19:4510–4516
13. Luo X, Wang X, Liao L, Gamboa S, Sebastian PJ (2006) Synthesis and characterization of high tap-density layered $Li[Ni_{1/3}Co_{1/3}Mn_{1/3}]O_2$ cathode material via hydroxide co-precipitation. J Power Sources 158:654–658
14. Yang X, Wang X, Wei Q, Shu H, Liu L, Yang S, Hu B, Song Y, Zou G, Hu L, Yi L (2012) Synthesis and characterization of a Li-rich layered cathode material $Li_{1.15}[(Mn_{1/3}Ni_{1/3}Co_{1/3})_{0.5}(Ni_{1/4}Mn_{3/4})_{0.5}]_{0.85}O_2$ with spherical core–shell structure. J Mater Chem 22:19666–19672
15. Chen WC, Song YF, Wang CC, Liu Y, Morris DT, Pianetta PA, Andrews JC, Wu HC, Wu NL (2013) Study on the synthesis–microstructure-performance relationship of layered Li-excess nickel–manganese oxide as a Li-ion battery cathode prepared by high-temperature calcinations. J Mater Chem A 1:10847–10856
16. Atebamba JM, Moskon J, Pejovnik S, Gaberscek M (2010) On the interpretation of measured impedance spectra of insertion cathodes for lithium-ion batteries. J Electrochem Soc 157:A1218–A1228